PHYSICAL REVIEW E **82**, 046309 (2010)

Development and validation of a turbulent-mix model for variable-density and compressible flows

Arindam Banerjee[*]
Department of Mechanical & Aerospace Engineering, Missouri University of Science & Technology, Rolla, Missouri 65409, USA

Robert A. Gore and Malcolm J. Andrews
Los Alamos National Laboratory, Los Alamos, New Mexico 87544, USA

(Received 21 June 2010; revised manuscript received 21 September 2010; published 21 October 2010)

The modeling of buoyancy driven turbulent flows is considered in conjunction with an advanced statistical turbulence model referred to as the BHR (Besnard-Harlow-Rauenzahn) *k-S-a* model. The BHR *k-S-a* model is focused on variable-density and compressible flows such as Rayleigh-Taylor (RT), Richtmyer-Meshkov (RM), and Kelvin-Helmholtz (KH) driven mixing. The BHR *k-S-a* turbulence mix model has been implemented in the RAGE hydro-code, and model constants are evaluated based on analytical self-similar solutions of the model equations. The results are then compared with a large test database available from experiments and direct numerical simulations (DNS) of RT, RM, and KH driven mixing. Furthermore, we describe research to understand how the BHR *k-S-a* turbulence model operates over a range of moderate to high Reynolds number buoyancy driven flows, with a goal of placing the modeling of buoyancy driven turbulent flows at the same level of development as that of single phase shear flows.

DOI: 10.1103/PhysRevE.82.046309 PACS number(s): 47.27.E−, 47.51.+a, 47.20.Ma

I. INTRODUCTION

Turbulence in complex, high speed, and high Reynolds number flows has been of intrinsic interest and research across many fields that include variable-density mixing. In particular, predictive capabilities for inertial confinement fusion (ICF) have relied on modeling the effects of material mixing, as well as enhanced momentum and thermal transport, induced by buoyancy driven turbulence. The focus of our work is to describe multimaterial, compressible, variable-density turbulence, and mixing in which different materials may or may not be initially mixed; with emphasis on flows that include Kelvin-Helmholtz (KH) [1,2], Rayleigh-Taylor (RT) [3,4], and Richtmyer-Meshkov (RM) Instabilities [5,6]. The potential applications of such flows range from laser driven ICF, where the mixing of the outer shell and the inner fluid results in a reduction of neutron yield [7,8], to applications such as supernova explosions [9], buoyant jets [10], atmospheric instability associated with cold air overlaying warm air in the atmosphere [11], oceanic overflow problems and also combustion applications where interaction of a shock wave with a flame results in deflagration-to-detonation transition [12]. All of the above applications involve fluid flows that are unsteady, with more than one material of differing density.

Turbulent mixing induced by buoyancy driven hydrodynamic instabilities has a number of distinct features compared with classical turbulent flows, that makes modeling of such flows extremely challenging. In particular, anisotropy and inhomogeneity resulting from initial and boundary conditions, a preferred direction due to acceleration, presence of shocks and material discontinuities, as well as baroclinic effects due to variable-density and vorticity production at material interfaces. Turbulence models that attempt to analyze and characterize these flows attend to issues associated with initialization of the turbulent field variables, which are considered as a serious problem for generalized turbulence theories [13]. Ideally, a good turbulence model should be able to mimic the early growth phase of the instability, followed by transition to turbulence, and the fully developed late time turbulent mixing stage. Traditionally, three different approaches have been taken when attempting to model buoyancy driven turbulence. The simplest (first) type of model uses ordinary differential equations for the width of the RT/RM mixing layer, where the bubble or spike amplitudes are described by balancing inertia, buoyancy and drag forces [14–17], so called "buoyancy-drag" models. However, such heuristic models have limited utility as they are not readily extended into two- or three-dimensions, and fail when there are multiple mixing interfaces whose amplitudes overlap. Demixing has been investigated [18–20] in a number of flows. Kucherenko *et al.* [20] as well as Smeeton and Youngs [18] accomplished this in RT flows by changing the acceleration during the self-similar growth stage of the turbulent mixing zone. In another example, Stafford [19] achieved unstable stratification by heating an initially stably stratified solution of water over saline solution, and then removed the heating. Buoyancy forces mixed the two fluids while heating was taking place, but once removed, a partial demixing was observed because the two fluids did not completely mix at the molecular level. Such problems have been addressed by a second type of models known as the two-fluid model [21–23]; in which each fluid has a velocity and a mass fraction. In these (two-fluid) models, a body force (gravity) induced different accelerations on each fluid fragment causing different fluid velocities, and hence, different drag on the

---

[*] Corresponding author; 292E Toomey Hall, Mechanical & Aerospace Engineering, Missouri S&T*, Rolla, MO 65409 (*formerly University of Missouri, Rolla); FAX: 573-341-6899; banerjeea@mst.edu

fluid fragments. Youngs [23,24] refers to this phenomenon as sifting and thus suggested the use of the two-fluid model to capture correctly the relative motion of the fluid fragments. A two-fluid model was deemed necessary, rather than a turbulence model that used a dissipation type gradient approximation for closure of the triple correlations, to capture the effects of a counter gradient mass/energy flux. Youngs [25] used a two-fluid model to investigate late-time turbulent mixing of RT instability and found good agreement with the rocket rig experiments [26]. Andrews [27,28] also used a similar two-fluid model to predict both the RT mixing width and late-time demixing. The two-fluid model was found to be necessary as the turbulent mixing layer comprised fragments of different density fluids, and tracking the individual fluids was key to predicting the demix process. It should be noted that the model described by Zhou *et al.* [17] is a hybrid model that is based on the buoyancy-drag and the two-scale concepts [29] and consisted of both the buoyancy drag and two-equations models. A third type of buoyancy driven turbulence model uses a Reynolds decomposition for a single field and maintains individual species mass fractions, but assigns a single velocity for the mixture [13,30–32]. Such models incorporate turbulent dissipation and are similar in complexity to multifluid models. Reasonable agreement with experiments is readily achieved with calibrated adjustment of turbulence model constants. Such models are able to handle multidimensions, multifluids, and variable accelerations; however, their results are not universal as model "constants" must be properly calibrated from experiments. In addition, such a gradient-diffusion based model cannot capture the demix process.

This paper describes validation studies for the single-point BHR turbulent-mix model. The BHR turbulent-mix model was introduced [33] as an adaptation of single-point engineering models for describing fluid flow involving large variations in density. Evolution equations were developed from second-order correlations and gradient-diffusion approximations were applied to close the system of equations. Using a mass weighted averaged decomposition, the original BHR model (Ref. [13], henceforth referred to as BHR92) included full transport equations for Reynolds stress tensor, turbulent mass flux, density fluctuations and the dissipation rate of the turbulence kinetic energy. The starting point for the BHR92 model was the Navier-Stokes equation, the continuity equation and the species transport equation. In particular, the species transport equation employed a Fickian model for molecular diffusion.

The goal of this paper is to simplify the model equations presented in BHR92 to a reduced model (henceforth referred to as the BHR *k*-*S*-*a*) that involve a turbulent kinetic energy, length scale and mass flux to describe instability-driven (KH, RT and RM) turbulence accurately. The different types of instabilities driven by pressure-gradients that are encompassed by the equations include RT instability; its shock-driven counterpart, RM instability; and shear driven instability, commonly known as KH instability. The model results are compared with a large test database available from experiments, and direct numerical simulations of RT, RM, and KH instabilities. The BHR *k*-*S*-*a* model is unique in the sense that it is the first effort to include all the three instabilities; i.e., KH, RT and RM. The *k*-*L* model of Dimonte and Tipton [30] does not fare well with KH instabilities. Gregoire *et al.* [34] reports the usage of their model only to RM instabilities. The rest of this paper is organized as follows. Section II describes the governing equations and the modeling inherent in BHR *k*-*S*-*a*. In Sec. III, the model equations are then evaluated based on a similarity solution technique that serves to baseline the model constants. The BHR *k*-*S*-*a* model simulations are then compared in Sec. IV with a large database of experiments and numerical simulations for RT [16,35,36], RM [37,38], and KH [39,40]. Section V closes the paper with conclusions and future directions of development for the BHR model.

II. GOVERNING EQUATIONS AND BHR MODEL REDUCTIONS

The usual convention of single-point turbulence modeling decomposes the flow field variables (density, ρ, velocity, u_i, and pressure, p) into mean and fluctuating quantities using Reynolds decomposition as

$$\rho = \bar{\rho} + \rho', \quad u_i = \bar{u}_i + u_i', \quad p = \bar{p} + p', \tag{1}$$

where the over bar denotes the uniformly weighted ensemble (time) average part and the prime denotes the fluctuating part. However, for variable-density flows, a mass-weighted averaging (Favre decomposition) procedure for the velocity is used which is defined as

$$u_i = \tilde{u}_i + u_i''; \quad \text{where} \quad \tilde{u}_i = \frac{\overline{\rho u_i}}{\bar{\rho}}, \tag{2}$$

u_i'' denotes the mass weighted fluctuation with $\overline{\rho u_i''}=0$. The Favre decomposition leads to a conservative form of the Reynolds stress tensor, R_{ij}, in the averaged momentum equations, where $R_{ij}=\overline{\rho u_i'' u_j''}$. The mass-weighted average velocity $\tilde{u}_i$ can be rewritten by applying the Reynolds decomposition to momentum density ρu_i as

$$\tilde{u}_i = \frac{\overline{\rho u_i}}{\bar{\rho}} = \bar{u}_i + \frac{\overline{\rho' u_i'}}{\bar{\rho}} = \bar{u}_i + a_i. \tag{3}$$

The quantity a_i $(=\overline{\rho' u_i'}/\bar{\rho})$ is the velocity associated with the mass-flux relative to a $\bar{u}_i$ frame of reference. A relationship between a_i and u_i'' can be established by inserting Favre and Reynolds decomposition into Eq. (5) and ensemble averaging to obtain,

$$a_i = -\overline{u_i''} \tag{4}$$

and $\bar{\rho} a_i$ is the turbulent mass flux. Another important quantity which appears in the current set of model equations is the density self correlation, b, defined as

$$b = -\overline{\rho' \left(\frac{1}{\rho}\right)'}. \tag{5}$$

Alternatively, because: $-\overline{\rho'(1/\rho)'} = +\overline{(\bar{\rho}-\rho)/\rho}$, then

$$b = \bar{\rho}\overline{\left(\frac{1}{\rho}\right)} - 1. \tag{6}$$

A third useful alternative is

$$b = -\overline{\rho'\left(\frac{1}{\bar{\rho}+\rho'} - \frac{1}{\bar{\rho}}\right)} = \overline{(\rho')^2/\rho\bar{\rho}}, \tag{7}$$

which implies that b is non-negative and that $b \approx \overline{(\rho')^2}/(\bar{\rho})^2$ at low Atwood number flows, i.e., if $\rho' \ll \bar{\rho}$. Based on these definitions, the generalized Reynolds stress tensor R_{ij} can be written as

$$R_{ij} = \overline{\rho u_i'' u_j''} = \bar{\rho}\overline{u_i' u_j'} - \bar{\rho} a_i a_j + \overline{\rho' u_i' u_j'}. \tag{8}$$

A set of transport equations for second-order correlations, namely turbulent mass-flux ($\bar{\rho} a_i$), density self correlation [Eq. (5)] and Reynolds stresses [Eq. (8)] are then derived from the Navier-Stokes equations. Gradient-type diffusion approximations developed from mean flow variables are applied to some, but not all, of the second and higher order correlations to provide an appropriate closure to the system of model equations [41–43]. For the purpose of this paper, it was assumed that the entire flow field is divergence free, since the applications discussed in this work are turbulent mixing of incompressible fluids which are driven by either of KH, RT or RM instabilities. Consequently, the internal energy equation is not discussed. For the incompressible case involving only two species, a species transport equation can be derived directly from conservation of mass equation [13,33,42].

A. Equation for turbulence kinetic energy and length scale

In the BHR92 model, a transport equation is derived for R_{ij}. This transport equation is derived in a rigorous, but unclosed form, from the Navier-Stokes equations. To construct a transport equation for R_{ij}, the variables are decomposed into mean and fluctuating parts using Favre decomposition, and transport equations from $\rho u_i''$ and u_i'' are derived. The two transport equations are multiplied by u_i'' and $\rho u_i''$, respectively, and the equations are added and ensemble averaged to create a transport equation for R_{ij}. Details about this derivation can be found elsewhere [13,33,44]. In the current work, instead of transporting the full Reynolds stress tensor R_{ij}, a transport equation for the turbulent kinetic energy per unit mass, k, is derived by using the definition: $R_{nn}=2\bar{\rho}k$ giving

$$\frac{\partial \bar{\rho} k}{\partial t} + \frac{\partial \bar{\rho} k \tilde{u}_n}{\partial x_n} = a_n \frac{\partial \bar{p}}{\partial x_n} - R_{nm}\frac{\partial \tilde{u}_m}{\partial x_n} + \frac{\partial}{\partial x_n}\left(\bar{\rho}\nu_t \frac{\partial k}{\partial x_n}\right) - \bar{\rho}\varepsilon. \tag{9}$$

From this transport equation for turbulent kinetic energy, dimensional arguments [13,33,42] can be used to establish a transport equation for the decay of turbulent kinetic energy, ε as

$$\frac{\partial \bar{\rho}\varepsilon}{\partial t} + \frac{\partial \bar{\rho}\varepsilon \tilde{u}_n}{\partial x_n} = C_{3\varepsilon}\frac{\varepsilon}{k} a_n \frac{\partial \bar{p}}{\partial x_n} - C_{1\varepsilon}\frac{\varepsilon}{k} R_{nm}\frac{\partial \tilde{u}_m}{\partial x_n} + C_{D\varepsilon}\frac{\partial}{\partial x_n}\left(\bar{\rho}\frac{k^2}{\varepsilon}\frac{\partial \varepsilon}{\partial x_n}\right) - C_{2\varepsilon}\bar{\rho}\frac{\varepsilon^2}{k}. \tag{10}$$

The k and the ε equations have been combined into a transport equation for length scale, S ($=k^{3/2}/\varepsilon$) and the resulting equation can be written as

$$\frac{\partial \bar{\rho} S}{\partial t} + \frac{\partial \bar{\rho} S \tilde{u}_n}{\partial x_n} = \frac{\partial}{\partial x_n}\left(\frac{\bar{\rho}\nu_t}{\sigma_\varepsilon}\frac{\partial S}{\partial x_n}\right) + \frac{S}{k}\left[\left(\frac{3}{2} - C_4\right) a_n \frac{\partial \bar{p}}{\partial x_n} - \left(\frac{3}{2} - C_1\right) R_{nm}\frac{\partial \tilde{u}_m}{\partial x_n}\right] - C_3 \bar{\rho} S \frac{\partial \tilde{u}_n}{\partial x_n} - \left(\frac{3}{2} - C_2\right)\bar{\rho}\sqrt{k}. \tag{11}$$

We have used both Eqs. (10) and (11) in our earlier studies and have found consistent results. In this work, we choose to use the S equation due to comparative ease in initialization and the use of ensuring self-similarity through $h \propto S$.

B. Equation for turbulent density-velocity correlation

The BHR92 model also transports the net mass flux velocity, a_i, which appears in the mean flow pressure gradient terms of the transport for R_{ij}, k, ε, and S. The transport equation for a_i is derived from the Navier-Stokes equations in rigorous, but unclosed form, and then closed through modeling. The equation for conservation of mass is multiplied by u' and the equation for conservation of momentum is multiplied by ρ'. The flow variables are then decomposed into mean and fluctuating parts, and the equations ensemble averaged (BHR92) to obtain a transport equation for $\overline{\rho' u'}$, namely,

$$\frac{\partial \overline{\rho' u_i'}}{\partial t} + \overline{u_i'\frac{\partial(\bar{\rho}u_n' + \rho'\tilde{u}_n + \rho' u_n')}{\partial x_n}} + \tilde{u}_n \overline{\rho'\frac{\partial u_i'}{\partial x_n}} + \overline{\rho' u_n'}\frac{\partial \tilde{u}_i}{\partial x} + \overline{\rho' u_n'\frac{\partial u_i'}{\partial t}} = -\overline{\left(\frac{\rho'}{\bar{\rho}+\rho'}\right)\frac{\partial(\bar{p}+p')}{\partial x_n}}. \tag{12}$$

The density-pressure correlation can be simplified as

$$-\overline{\left(\frac{\rho - \bar{\rho}}{\bar{\rho}+\rho'}\right)\frac{\partial(\bar{p}+p')}{\partial x_n}} = \left[\bar{\rho}\overline{\left(\frac{1}{\rho}\right)} - 1\right]\frac{\partial \bar{p}}{\partial x_n} + \bar{\rho}\overline{\left(\frac{1}{\rho}\right)\frac{\partial p'}{\partial x_n}} = b\frac{\partial \bar{p}}{\partial x_n} + \bar{\rho}\overline{\left(\frac{1}{\rho}\right)\frac{\partial p'}{\partial x_n}}. \tag{13}$$

The resulting unmodeled transport equation for a_i becomes

$$\frac{\partial \bar{\rho} a_i}{\partial t} + \frac{\partial \bar{\rho} a_i \tilde{u}_n}{\partial x_n} = b\frac{\partial \bar{P}}{\partial x_i} - \frac{R_{in}}{\bar{\rho}}\frac{\partial \bar{\rho}}{\partial x_n} + \bar{\rho}\frac{\partial a_i a_n}{\partial x_n} - \bar{\rho} a_n \frac{\partial(\tilde{u}_i - a_i)}{\partial x_j} + \bar{\rho}\left(\overline{\mathrm{v}'\frac{\partial P'}{\partial x_i}} - \overline{\mathrm{v}'\frac{\partial \tau'_{in}}{\partial x_n}}\right) - \overline{\bar{\rho} u'_i \frac{\partial u'_n}{\partial x_i}} - \rho\frac{\partial}{\partial x_n}\left(\frac{\overline{\rho' u'_i u'_n}}{\bar{\rho}}\right). \tag{14}$$

In BHR, a gradient-diffusion approximation is used to model the triple correlations as

$$\overline{\rho' u'_i u'_n} = -\frac{\rho \nu_T}{\sigma_a}\frac{\partial a_i}{\partial x_n}. \tag{15}$$

The modeling of the density-pressure correlation of the a_i equation is split into two parts: the first part corresponds to the mean flow gradients, and the second part represents a decay term of a_i. With the above modeling assumptions, the transport equation for a_i in the BHR *k-S-a* model becomes

$$\frac{\partial \bar{\rho} a_i}{\partial t} + \frac{\partial \bar{\rho} a_i \tilde{u}_n}{\partial x_n} = b\frac{\partial \bar{P}}{\partial x_i} - \frac{R_{in}}{\bar{\rho}}\frac{\partial \bar{\rho}}{\partial x_n} + \bar{\rho}\frac{\partial a_i a_n}{\partial x_n} - \bar{\rho} a_n \frac{\partial(\tilde{u}_i - a_i)}{\partial x_n} + \frac{\partial}{\partial x_n}\left(\frac{\rho \nu_T}{\sigma_a}\frac{\partial a_i}{\partial x_n}\right) - \frac{C_{a1}\bar{\rho}\sqrt{k}}{S}a_i. \tag{16}$$

C. Equation for density self-correlation

The density self-correlation, b, is coupled to the principal driving term in the a_i equation [fourth term of RHS of Eq. (16)]. A transport equation for b is derived by using the Reynolds decomposition on the equation for specific volume, υ ($=1/\rho$) derived from the conservation of mass equation as

$$\frac{\partial \bar{\upsilon}}{\partial t} + \overline{u_n}\frac{\partial \bar{\upsilon}}{\partial x_n} = \bar{\upsilon}\frac{\partial \overline{u_n}}{\partial x_n} + \overline{\upsilon'\frac{\partial u'_n}{\partial x_n}} - \overline{u'_n\frac{\partial \upsilon'}{\partial x_n}}. \tag{17}$$

Substituting Eq. (5), an exact transport equation for b is obtained, which on simplification can be written as

$$\frac{\partial b}{\partial t} + \overline{u_n}\frac{\partial b}{\partial x_n} = -\frac{b+1}{\bar{\rho}}\frac{\partial \bar{\rho} a_n}{\partial x_n} - \bar{\rho}\frac{\partial \overline{u'_n \upsilon'}}{\partial x_n}. \tag{18}$$

BHR92 modeled the velocity-specific volume correlation term [first term on RHS of Eq. (18)] as a gradient-diffusion term, and the specific-volume-velocity gradient correlation term was modeled as a dissipation term. The BHR92 b equation is thus of the form

$$\frac{\partial b}{\partial t} + \overline{u_n}\frac{\partial b}{\partial x_n} = -\frac{b+1}{\bar{\rho}}\frac{\partial \bar{\rho} a_n}{\partial x_n} + \frac{\partial}{\partial x_n}\left(\frac{\bar{\rho}\nu_t}{\sigma_b}\frac{\partial b}{\partial x_n}\right) - C_{1b}\frac{\sqrt{k}}{S_b}b. \tag{19}$$

For the current study we assume no interspecies diffusion (two separate fluids), so the b equation has no decay term. Consequently, the b equation is replaced by two-fluid expression for b [44],

$$b = \frac{\alpha_1 \alpha_2 (\rho_1 - \rho_2)^2}{\rho_1 \rho_2}. \tag{20}$$

D. Equation for conservation of species

The ensemble average equation for species α interdiffusing in a mixture is obtained from conservation of mass by applying Fick's law of diffusion with a constant diffusion coefficient D, and separating the variables into mean and fluctuating components. The ensemble average unmodeled equation for the mass fraction of species α, c_α is

$$\frac{\partial \bar{\rho}\tilde{c}_\alpha}{\partial t} + \frac{\partial \bar{\rho}\tilde{u}_n\tilde{c}_\alpha}{\partial x_n} + \frac{\partial}{\partial x_n}\overline{\rho u''_n c''_\alpha} = \frac{\partial}{\partial x_n}\left(\bar{\rho} D\frac{\partial \tilde{c}_\alpha}{\partial x_n}\right) + \frac{\partial}{\partial x_n}\left(\overline{\rho D\frac{\partial}{\partial x_n}c''_\alpha}\right). \tag{21}$$

Once again, we identify that the last term on the left hand side of Eq. (24) denotes turbulent diffusion of mass fraction and can be modeled as follows:

$$\frac{\partial}{\partial x_n}\overline{\rho u''_n c''_\alpha} = -\frac{\partial}{\partial x_n}\left(\frac{\bar{\rho}\nu_t}{\sigma_c}\frac{\partial \tilde{c}_\alpha}{\partial x_n}\right). \tag{22}$$

Therefore, using the modeled term in [25] and assuming that molecular diffusivity is negligible, the modeled version for species is written as

$$\frac{\partial \bar{\rho}\tilde{c}_\alpha}{\partial t} + \frac{\partial \bar{\rho}\tilde{u}_n\tilde{c}_\alpha}{\partial x_n} = \frac{\partial}{\partial x_n}\left(\frac{\bar{\rho}\nu_t}{\sigma_c}\frac{\partial \tilde{c}_\alpha}{\partial x_n}\right). \tag{23}$$

E. Simplified BHR (k-S-a) model equations

Implementation of Eqs. (9), (11), (16), and (20) in a multidimensional hydrodynamic code is tedious. Therefore, it is of interest to simplify the BHR92 model equations; one such simplification is undertaken in the current work to incorporate the BHR *k-S-a* model equations in the RAGE hydrocode [45]. The 1D BHR model equations solved by RAGE are as follows:

$$\frac{\partial \bar{\rho}}{\partial t} + \frac{\partial \bar{\rho}\tilde{u}}{\partial z} = 0, \tag{24a}$$

$$\frac{\partial \bar{\rho}\tilde{u}}{\partial t} + \frac{\partial \bar{\rho}\tilde{u}^2}{\partial z} = -\frac{\partial}{\partial z}(\bar{p} + R_{zz}) + \bar{\rho} g, \tag{24b}$$

$$\frac{\partial \bar{\rho} k}{\partial t} + \frac{\partial \bar{\rho} k\tilde{u}}{\partial z} = a\frac{\partial \bar{p}}{\partial z} - R_{zz}\frac{\partial \tilde{u}}{\partial z} + \frac{\partial}{\partial z}\left(\bar{\rho}\nu_t\frac{\partial k}{\partial z}\right) - \bar{\rho}\varepsilon, \tag{24c}$$

$$\frac{\partial \bar{\rho} a}{\partial t} + \frac{\partial \bar{\rho} a\tilde{u}}{\partial z} = b\frac{\partial \bar{p}}{\partial x_i} - \frac{R_{zz}}{\bar{\rho}}\frac{\partial \bar{\rho}}{\partial z} - C_{a1}\frac{\bar{\rho} a\sqrt{k}}{S}, \tag{24d}$$

$$\frac{\partial \bar{\rho} S}{\partial t} + \frac{\partial \bar{\rho} S\tilde{u}}{\partial z} = \frac{S}{k}\left[\left(\frac{3}{2} - C_4\right)a\frac{\partial \bar{p}}{\partial z} - \left(\frac{3}{2} - C_1\right)R_{zz}\frac{\partial \tilde{u}}{\partial z}\right] - C_3\bar{\rho} S\frac{\partial \tilde{u}}{\partial z} + \frac{\partial}{\partial z}\left(\frac{\bar{\rho}\nu_t}{\sigma_\varepsilon}\frac{\partial S}{\partial z}\right) - \left(\frac{3}{2} - C_2\right)\bar{\rho}\sqrt{k}, \tag{24e}$$

$$b = \frac{\alpha_1\alpha_2(\rho_1-\rho_2)^2}{\rho_1\rho_2}, \tag{24f}$$

$$\frac{\partial\bar\rho\tilde c_\alpha}{\partial t} + \frac{\partial\bar\rho\tilde u\tilde c_\alpha}{\partial z} = \frac{\partial}{\partial z}\left(\frac{\bar\rho\nu_t}{\sigma_c}\frac{\partial\tilde c_\alpha}{\partial z}\right); \quad \nu_t = C_\mu S\sqrt{k}; \quad \varepsilon = k^{3/2}/S,$$

$$R_{ij} = \frac{2}{3}\left(\bar\rho k - 2\bar\rho\nu_t\frac{\partial\tilde u}{\partial z}\right); \quad \bar\rho = \alpha_1\rho_1 + \alpha_2\rho_2; \quad \alpha_1+\alpha_2 = 1. \tag{24g}$$

The BHR *k*-*S*-*a* model Eqs. (24a)–(24g) may be considered a variable-density extension of the more traditional *k*-ε model, coupled with a modeling methodology suitable for variable-density flows.

F. About RAGE with mix

RAGE (Radiation Adaptive Grid Eulerian) is a three-dimensional multimaterial Eulerian radiation hydrodynamics code developed Los Alamos National Laboratory and SAIC (Science Applications International Corporation). RAGE uses a continuous (in time and space) adaptive-mesh-refinement (CAMR) algorithm to follow interfaces and shocks, and gradients of physical quantities such as material densities and temperatures. RAGE incorporates a second-order-accurate Godunov hydrodynamics scheme, and is a fully compressible code. Here we have set the code to a one-dimensional Cartesian geometry to mimic both flows considered here. All materials defined in a multimaterial problem are present in each cell, and the code conserves mass, momentum and energy. The transport equations of the BHR *k*-*S*-*a* model [Eq. (24)] have been implemented in RAGE with *K*, *S*, *a* and c_α being the transported model variables. The mass, momentum, and internal energy in RAGE are then updated by incorporating the effects of turbulent diffusion on each quantity such that

$$\frac{\partial\bar\rho c_\alpha}{\partial t} + \nabla\cdot(\bar\rho c_\alpha\tilde u) = \nabla\cdot\left(\frac{\bar\rho\nu_t}{\sigma_c}\nabla c_\alpha\right),$$

$$\frac{\partial\bar\rho\tilde u}{\partial t} + \nabla\cdot(\bar\rho\tilde u\tilde u) = -\nabla\bar p + \nabla\cdot R, \tag{25}$$

where: $\bar\rho c_\alpha = (\frac{M}{V})(\frac{m_\alpha}{M}) = \frac{m_\alpha}{V}$; $\Sigma\frac{m_\alpha}{V} = \bar\rho$; M=total mass and V=total volume. The current model uses a one-dimensional validation for KH, RT, and RM instabilities. The initial conditions used in our BHR *k*-*S*-*a*/RAGE simulations are important for comparing the model simulations with experimental or DNS data sets. The current work used initial top-hat profiles for *k* and *S*. The mass-flux velocity, *a*, was zero at the start of the run.

III. EVALUATION OF BHR *k*-*S*-*a* MODEL CONSTANTS

Here we describe a one-dimensional self-similar solution for the low Atwood number Rayleigh Taylor experiments of Banerjee *et al.* [35]. The solution method is similar to the one used by Andrews [27,28], Spitz and Haas [46], Snider and Andrews [32]. In the low Atwood number gas channel experiment [47], two gas streams, one containing air and the other a helium-air mixture, flow parallel to each other at the same velocity separated by a thin splitter plate. The streams meet at the end of the splitter plate leading to formation of an unstable interface, and thereafter buoyancy driven mixing. The BHR model equations may be readily simplified to describe a low A_t=0.04 air-helium experiment. The mean vertical and horizontal velocities are set to zero in a Galilean frame moving with the mean velocity (i.e., $\bar u = \bar v = 0$), and from the low Atwood hot-wire measurements [35,48], we know that $\overline{\rho' u'} \approx 0$, and similarly $\overline{\rho' v'} \approx 0$. Consequently, the mass averaged horizontal velocities: $\tilde u = \bar u + \frac{\overline{\rho' u'}}{\bar\rho} \approx 0$ and $\tilde v \approx 0$. The mass averaged vertical velocity fluctuation can be written as a normalized mass flux in the vertical direction: $\tilde w = \tilde w + \frac{\overline{\rho' w'}}{\bar\rho} = \frac{\overline{\rho' w'}}{\bar\rho} = a_z$. The Reynolds stress tensor can be written as

$$R = \begin{pmatrix} \frac{2}{3}\bar\rho k + \frac{2}{3}\bar\rho\nu_t\frac{\partial\tilde w}{\partial z} & 0 & 0 \\ 0 & \frac{2}{3}\bar\rho k + \frac{2}{3}\bar\rho\nu_t\frac{\partial\tilde w}{\partial z} & 0 \\ 0 & 0 & \frac{2}{3}\bar\rho k - \frac{4}{3}\bar\rho\nu_t\frac{\partial\tilde w}{\partial z} \end{pmatrix}. \tag{26}$$

The model Eqs. (24c)–(24e) thus reduce to

$$\frac{\partial k}{\partial t} + \frac{\partial(ka_z)}{\partial z} = \frac{a_z}{\bar\rho}\left(\frac{\partial\bar p}{\partial z}\right) - \frac{2k}{3}\frac{\partial a_z}{\partial z} + \frac{4\nu_t}{3}\left(\frac{\partial a_z}{\partial z}\right)^2 + \frac{\partial}{\partial z}\left(\nu_t\frac{\partial k}{\partial z}\right) - \frac{k^{3/2}}{S}, \tag{27}$$

$$\begin{aligned}\frac{\partial S}{\partial t} + \frac{\partial(Sa_z)}{\partial z} = {} & \frac{S}{k}\left(\frac{3}{2} - C_4\right)\frac{a_z}{\bar\rho}\frac{\partial\bar p}{\partial z} - \frac{2S}{3}\left(\frac{3}{2} - C_1\right)\frac{\partial a_z}{\partial z} \\ & + \frac{4S\nu_t}{3k}\left(\frac{3}{2} - C_1\right)\left(\frac{\partial a_z}{\partial z}\right)^2 - C_3 S\frac{\partial a_z}{\partial z} \\ & + \frac{\partial}{\partial z}\left(\frac{\nu_t}{\sigma_\varepsilon}\frac{\partial S}{\partial z}\right) - \left(\frac{3}{2} - C_2\right)\sqrt{k},\end{aligned} \tag{28}$$

$$\frac{\partial a_z}{\partial t} + \frac{\partial a_z^2}{\partial z} = b\frac{\partial\bar p}{\partial z} - \frac{2k}{3\bar\rho}\frac{\partial\bar\rho}{\partial z} + \frac{4\nu_t}{3\bar\rho}\frac{\partial a_z}{\partial z}\frac{\partial\bar\rho}{\partial z} - C_{a1}\frac{a_z\sqrt{k}}{S}. \tag{29}$$

The species transport equation is recast in terms of density as

$$\frac{\partial\rho}{\partial t} + \frac{\partial}{\partial z}(a_z\bar\rho) = \frac{\partial}{\partial z}\left(\frac{\nu_t}{\sigma_t}\frac{\partial\bar\rho}{\partial z}\right). \tag{30}$$

Initial conditions are as follows

$$\text{at} \quad t=0 \quad \text{for} \quad z \geq 0; \quad \bar\rho = \rho_2, \quad k=0, \quad S=0, \quad a_z=0,$$

$$\text{at}\quad t=0\quad \text{for}\quad z<0;\quad \bar{\rho}=\rho_1,\quad k=0,\quad S=0,\quad a_z=0.$$

Exterior quiescent fluid boundary conditions are applied at the mixing layer boundary as

$$\text{for}\quad z>h_b;\quad \bar{\rho}=\rho_2,\quad k=0,\quad S=0,\quad a_z=0,$$

$$\text{for}\quad z<-h_s;\quad \bar{\rho}=\rho_1,\quad k=0,\quad S=0,\quad a_z=0.$$

The set of Eqs. (30)–(32) have self-similar solutions using the similarity variables,

$$\eta=\frac{z}{t^2};k(t,z)=t^2\hat{k}(\eta);S(t,z)=t^2\hat{S}(\eta),\ \ b(t,z)=\hat{b}(\eta),$$

$$\bar{\rho}(t,z)=\hat{\rho}(\eta),\ \ a_y(t,z)=t\hat{a}_y(\eta).$$

Substituting similarity variables into Eqs. (30)–(32), the following ordinary differential equations for $\hat{k},\hat{S}$ and $\hat{a}_z$ are obtained as

$$2\hat{k}-2\eta\frac{d\hat{k}}{d\eta}+\frac{d(\hat{k}\hat{a}_z)}{d\eta}=\hat{a}_zg-\frac{2\hat{k}}{3}\frac{d\hat{a}_z}{d\eta}+\frac{4C_\mu\hat{S}\hat{k}^{1/2}}{3}\frac{d\hat{a}_z}{d\eta}+C_\mu\frac{d}{d\eta}\left(\hat{S}\hat{k}^{1/2}\frac{d\hat{k}}{d\eta}\right)-\frac{\hat{k}^{3/2}}{\hat{S}},\tag{31}$$

$$\begin{aligned}2\hat{S}-2\eta\frac{d\hat{S}}{d\eta}+\frac{d(\hat{S}\hat{a}_z)}{d\eta}={}&\frac{\hat{S}\hat{a}_zg}{\hat{k}}\left(\frac{3}{2}-C_4\right)-\frac{2\hat{S}}{3}\left(\frac{3}{2}-C_1\right)\frac{d\hat{a}_z}{d\eta}\\&+\frac{4C_\mu\hat{S}^2}{3\hat{k}^{1/2}}\left(\frac{3}{2}-C_1\right)\left(\frac{d\hat{a}_z}{d\eta}\right)^2-C_3\hat{S}\frac{d\hat{a}_z}{d\eta}\\&+\frac{C_\mu}{\sigma_\varepsilon}\frac{d}{d\eta}\left(\hat{S}\hat{k}^{1/2}\frac{d\hat{S}}{d\eta}\right)-\left(\frac{3}{2}-C_2\right)\hat{k}^{1/2},\end{aligned}\tag{32}$$

$$\hat{a}_z-2\eta\frac{d\hat{a}_z}{d\eta}+\frac{d\hat{a}_z^2}{d\eta}=bg-\frac{2\tilde{k}}{3\bar{\rho}}\frac{d\hat{\rho}}{d\eta}+\frac{4C_\mu\hat{S}\hat{k}^{1/2}}{3\bar{\rho}}\frac{d\hat{a}_z}{d\eta}\frac{d\hat{\rho}}{d\eta}-C_{a1}\frac{\hat{a}_z\hat{k}^{1/2}}{\tilde{S}}.\tag{33}$$

The equations may be integrated by assuming approximate profiles chosen to represent $\hat{k},\hat{S},\hat{a}_z$ and $\hat{\rho}$. Here, we choose to represent the turbulent kinetic energy and mass flux as approximated by a parabolic profile, and density within the mixing layer is approximated by a linear profile [48]. It is shown later that these profiles are reasonable approximations to actual profiles obtained from experiments. The approximate profiles are

$$\tilde{k}=C_k(1-\tilde{\eta}^2),\quad \tilde{S}=C_S(1-\tilde{\eta}^2)^{1/2},\quad \tilde{a}=C_a(1-\tilde{\eta}^2),$$

$$\tilde{\rho}=C_\rho\tilde{\eta}+\tilde{\rho}_1,$$

where the length-scale is normalized based on the mixing half width, $C_w=h_{b,s}/t^2$,

$$\tilde{\eta}=\frac{\eta}{C_w}=\frac{z}{h_{b,s}}$$

C_k, C_S, and C_a are constants. For the linear density profile, $C_\rho=\frac{\rho_2-\rho_1}{2}=-\frac{\Delta\rho}{2}$ and $\tilde{\rho}_1=\frac{\rho_2+\rho_1}{2}$, where $A_t=\frac{\rho_1-\rho_2}{\rho_1+\rho_2}$. The self-similar form of the equations is integrated across the mixing layer from $-1<\tilde{\eta}<1$ and the constants are calculated from the algebraic relationships,

$$4C_k+\frac{C_k^{3/2}}{C_S}=C_ag+\frac{16}{15}C_\mu C_SC_k^{1/2}C_a^2,\tag{34}$$

$$4C_S+\left(\frac{3}{2}-C_2\right)C_k^{1/2}=\left(\frac{3}{2}-C_4\right)\frac{C_SC_ag}{C_k}+\frac{4}{3}\left(\frac{3}{2}-C_1\right)\frac{C_\mu C_S^2C_a^2}{C_w^2C_k^{1/2}},\tag{35}$$

$$C_{a1}=\frac{C_S}{C_aC_k^{1/2}}\left[\frac{3}{2}C_bg-\frac{2C_kC_\rho}{3C_w\bar{\rho}}-3C_a\right].\tag{36}$$

TABLE I. BHR constants for KH-RT-RM flows set by an iterative match to mainly compressible experiments. The constants listed under Gas Channel [35] were evaluated using a self-similar solution technique.

	KHI	RTI			RMI	
Model constants	BM [39]	Gas Channel [35]	LEM [16]	DNS [36]	Poggi [37]	VS [38]
C_1	1.44	1.44	1.25	1.44	1.44	1.44
C_2	1.92	1.92	1.92	1.92	1.92	1.92
C_3	0	0	0	0	0	0
C_4	0.58	0.58	0.80	0.80	0.58	0.58
C_μ	0.28	0.28	0.09	0.28	0.28	0.28
C_{a1}	7.0	7.0	2.25	7.0	7.0	7.0
C_{a2}	0.25	0.25	1.0	0.20	0.2	0.2
σ_ε	0.1	0.1	0.1	0.1	0.1	0.1
σ_c	0.6	0.6	0.6	0.6	0.6	0.6

The constants C_4, C_μ, $C_{\mathrm{a}1}$, and $C_{\mathrm{a}2}$ (see Table I) are evaluated based on measurements of k, a, b, and h from the air-helium $A_{\mathrm{t}}=0.4$ experiments [35,48]. In addition, C_1 was set based on nominal shear layer growth rate, C_2 was based on nominal decay rate in homogeneous turbulence, and σ_ε was based on the profiles of S from Ristorcelli and Clark [49]. The BHR k-S-a/RAGE simulations are initialized with reasonable initial values of $k_0=1\ \mathrm{cm}^2/\mathrm{s}^2$ and $S_0=0.1\ \mathrm{cm}$ with top-hat distributions across an initial mixing width for all the cases. The value of a at the start of the simulation is always zero. For majority of the RANS type models, the values of the initial conditions are usually considered to be not important for RT and KH. However, we believe that a proper characterization of initial conditions is important for direct comparison of the BHR results with KH experiments, RT experiments and direct numerical simulations (DNS) and transient RM experiments. However, if the Reynolds number

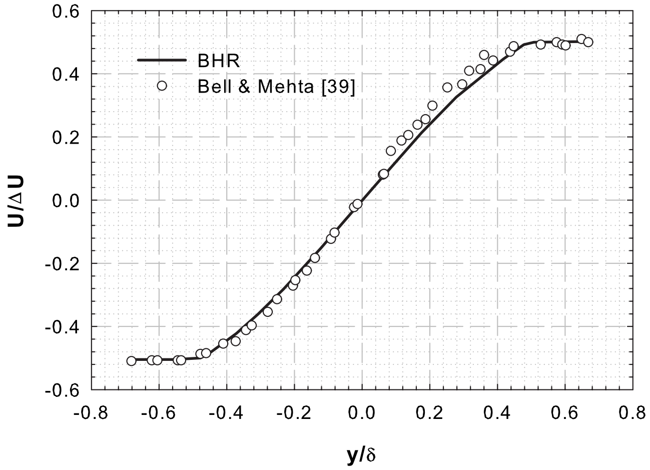

FIG. 1. Mean stream-wise velocity profiles: comparison of the experiments from Bell and Mehta [39] with BHR/RAGE model simulations.

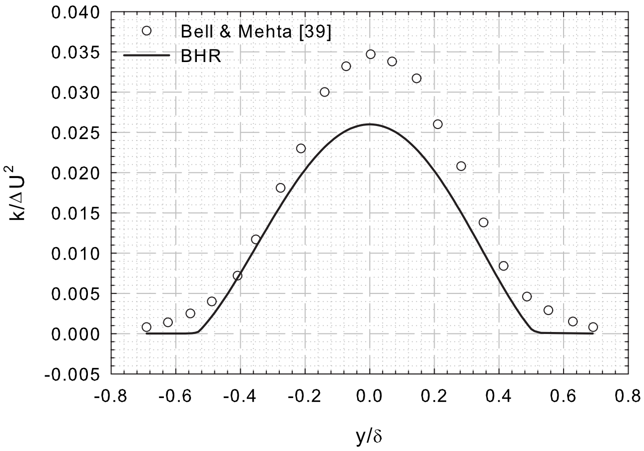

FIG. 2. Comparison of the turbulence kinetic energy (k) for the experiments of Bell and Mehta [39] with BHR/RAGE model simulations.

at the start of the calculation is sufficiently large, then initial conditions seeded into the flow has little role in our BHR-RAGE calculations. On-going work is seeking to capture the time-dependent transition to turbulence as detailed in the works of Zhou [50] and co-workers [51,52].

IV. COMPARISON OF BHR RESULTS WITH EXPERIMENTAL AND NUMERICAL DATA SETS

A. KH instability: Comparison with low-speed shear flows

Next, we describe how the BHR *k-S-a* model is tested for its ability to describe KH instability (shear flows). The low speed air/air shear layer set-up of Bell & Mehta [39] was used for comparison. The free-stream velocity of the two streams was 15 and 9 m/s, thus giving a velocity ratio of 0.6. The model simulations are initialized with the value of the initial length-scale, S_0, corresponding to the boundary layer thickness (δ_{99}) at the end of the splitter plate [39]. The BHR *k-S-a* model results for the mean stream-wise velocity profiles, normalized by the velocity deficit between the two streams, are compared with the experiment in Fig. 1, and the comparison reveals a good agreement. Figure 2 compares the profile of turbulence kinetic energy (k) from the model with the experiment. Although the model simulations were initialized with the same initial length scale (S_0), there seems to be a mismatch between the experimental data and BHR *k-S-a* results at the center line that we attribute to incomplete characterization of the initial conditions in the flow.

B. RT instability (buoyancy driven flow)

The BHR *k-S-a* model was tested for its ability to describe RT instability driven fluid mixing with constant acceleration. The model constants were calculated from the low Atwood number (A_t=0.04) statistically steady RT experimental data sets of Banerjee *et al.* [35], using the analytical self-similar solution of the model equations of [30]. The evaluated model constants were then used in BHR *k-S-a*/RAGE simulations and the results compared with RT experimental and simulation data [16,35,36]. Upon validation at low Atwood number flows (A_t=0.04), the BHR model was then used to model the high Atwood number experiments ($0.1<A_t<0.9$) of Dimonte and Schneider [16], and the numerical simulations (DNS at A_t=0.5) of Cabot and Cook [36]. Our attempts to use the model over such wide range of Atwood numbers (0.04 to 0.9) posed several challenges are described next.

1. Comparison with low Atwood number RT experiments

The low Atwood number RT experimental data obtained in the air-helium gas channel facility of [35,47] was used as a foundation data set to calibrate the BHR *k-S-a* model equations in RT flow. In the experiment, two gas streams, one containing air and the other containing helium-air mixture, flow parallel to each other separated by a thin splitter plate. The streams meet at the end of a splitter plate leading to the formation of an unstable interface and of buoyancy driven mixing. This buoyancy driven mixing experiment allows for long data collection times, short transients, and is statistically steady. The statistically steady RT setup provides large statistical data sets using hot-wire anemometry [16,35,36] to obtain Reynolds stresses, mix profiles, velocity-density correlations, and measures of molecular mixing. Numerical simulations were performed with two fluids with constant densities of $\rho_1=1.0833$ g/cm^3 and $\rho_2=1.0$ g/cm^3, that matched the experiment. Model constants were evaluated using self-similar solutions of the model equations as described above, and the model results compared with the experiment to facilitate model constant evaluation.

The following comparisons are made once the flow has attained self-similarity. The computed volume fraction profiles are compared with the Gas Channel measurements at A_t=0.04 in Fig. 3. The model shows a linear variation for the volume fraction across the RT mixing layer, with slight rounding at the edges (within the limits of the experimental errors) attributed to the shape of the plumes at the RT mix edge, and it compares well with the experimental volume fraction profiles. Scaled turbulence kinetic energy profiles

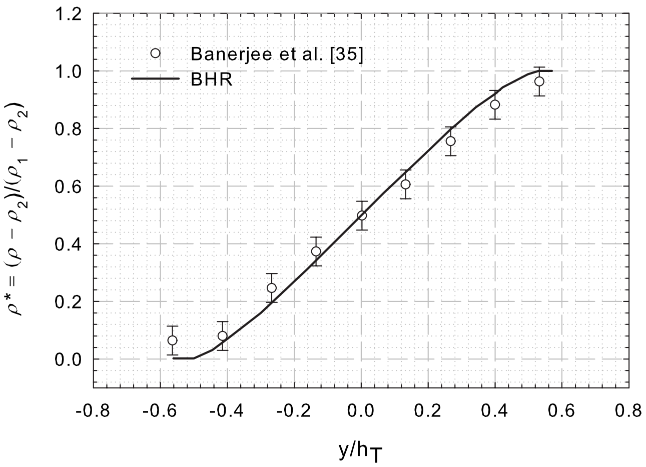

FIG. 3. Comparison of the BHR volume fraction profiles with the low Atwood number experimental data of Banerjee *et al.* [35].

$k^*[=k/(A_t g t)^2]$ across the mix are compared in Fig. 4. The figure shows that computed and experimentally measured profiles of k are approximately parabolic with a peak centered at the geometric centerline of the RT mixing layer. Similar parabolic profiles are observed for the plots of mass flux (drift) velocity, $a^*(=a/A_t g t)$, as seen in Fig. 5. Both Figs. 4 and 5 show reasonable agreement between the experiments and BHR *k-S-a* simulations, with the peak centerline values being underpredicted perhaps due to initial condition uncertainty. The density self-correlation, b, across the mix is plotted in Fig. 6. The current work uses a two-fluid expression for b [see Eq. (23)] and good agreement is obtained between the model simulations and experimental measurements, thus justifying our assumption of neglecting interspecies diffusion in the b equation (the decay term is in balance with the production term). The gas channel experiment of [35] has no shear; gravity drives the vertical velocity fluctuations, generating the characteristic "mushroom" shape of a Rayleigh-Taylor instability, and so w′ dominates over u' everywhere across the RT mixing layer. The measured w′/u' ratio across the RT mixing layer is plotted in Fig. 7, and is approximately constant across the RT mixing layer at ~1.8. This suggests an existing equilibrium between u' and the w′ kinetic energy production terms everywhere in the RT mixing layer; the mushroom shaped structures are convected up and down the RT mixing layer with little or no change in shape [35]. Since the BHR *k-S-a* model equations calculates turbulence kinetic energy and not the individual components of velocity, it assumes isotropy and the ratio w′/u' obtained from the BHR *k-S-a* simulations ~1 as seen in Fig. 7 [49,53].

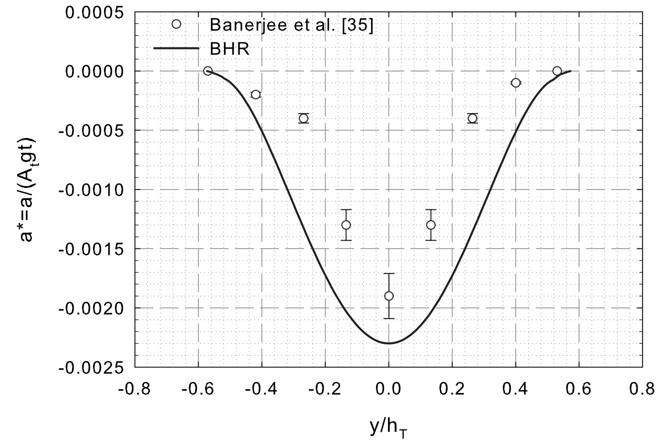

FIG. 5. Comparison of the normalized turbulent mass flux velocity profiles of the BHR simulations with the low Atwood number experimental data of Banerjee *et al.* [35].

2. Comparison with high Atwood number RT experiments

The BHR *k-S-a* model is next compared with the high Atwood number LEM (linear electric motor) experiments [16]. Since the LEM data set covers a large range of Atwood numbers ($0.13 \leq A_t \leq 0.96$) and is for immiscible fluids, $C_{a2} = 1.0$ and the model constants were modified based on the self-similar symmetric solutions (see Table I) for measured bubble penetration observed for large Atwood number runs, i.e., for $A_t > 0.5$. The model constants used here were based on historical values used in the earlier works. Universality

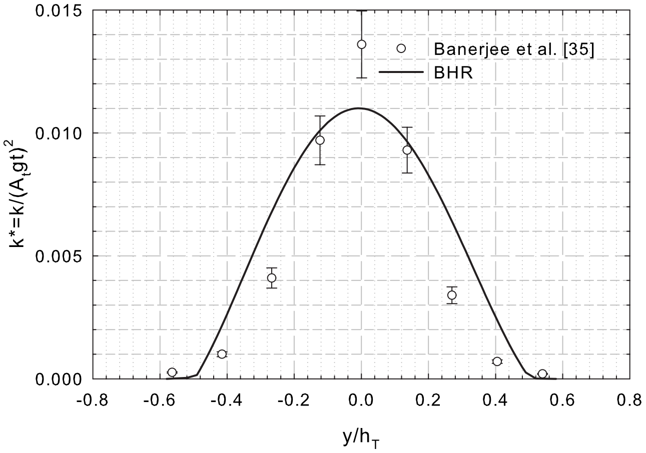

FIG. 4. Comparison of the normalized turbulent kinetic energy profiles of the BHR simulations with the low Atwood number experimental data of Banerjee *et al.* [35].

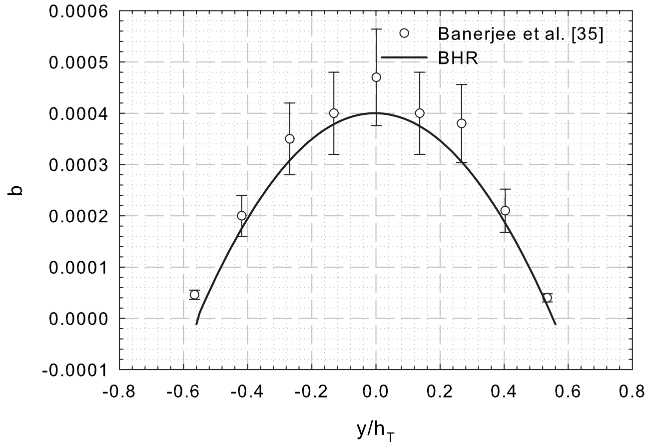

FIG. 6. Comparison of the density self correlation profiles of the BHR simulations with the low Atwood number experimental data of Banerjee *et al.* [35].

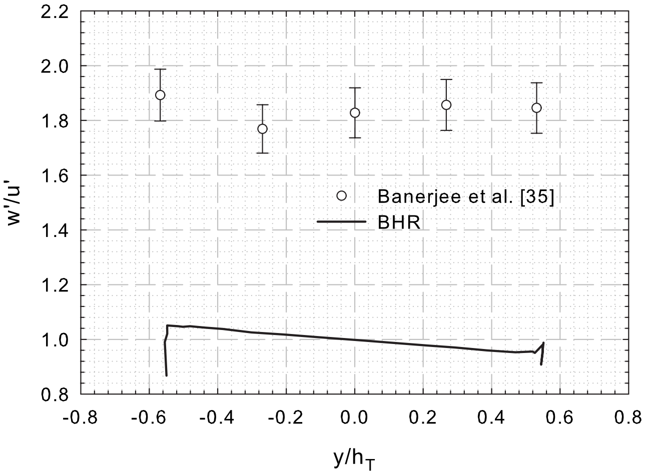

FIG. 7. Comparison of the ratio of velocity fluctuations (w′/u′) of the BHR simulations with the low Atwood number experimental data of Banerjee *et al.* [35].

may be arrived at with, perhaps, coefficients based on a Schmidt number. Figures 8(a) and 8(b) compares the volume fraction profiles at $A_t = 0.2$ and 0.32 obtained from the BHR *k-S-a* simulations with the LEM data. The comparison reveals that both cases give good agreement between experiment and model simulations. Next the variation in α_b and α_s with the Atwood number is compared with the LEM observations (see Fig. 9). α_s is consistent with the LEM data. However, the value of α_b from LEM experimental data was approximately constant over $0.13 \leq A_t \leq 0.96$. The BHR *k-S-a* simulations exhibit a slight increase in α_b at $A_t > 0.7$. The difference may be attributed to measurement uncertainties in the LEM experimental data [16]. Figure 10 plots the ratio of α_s/α_b as a function of the density ratio ρ_h/ρ_l. This is done to exhibit a simple dependence of α_s with ρ_h/ρ_l, and shows a dependence of α_s with ρ_h/ρ_l rather than Atwood number. The BHR model shows good agreement with experimental results ($\alpha_s/\alpha_b \sim 2$) up to $\rho_h/\rho_l = 10$ ($A_t = 0.81$). For $\alpha_s/\alpha_b > 2$, the comparison between BHR *k-S-a* and LEM data are moderate due to the mismatch in the bubble amplitudes and the large uncertainty reported in the LEM experimental data.

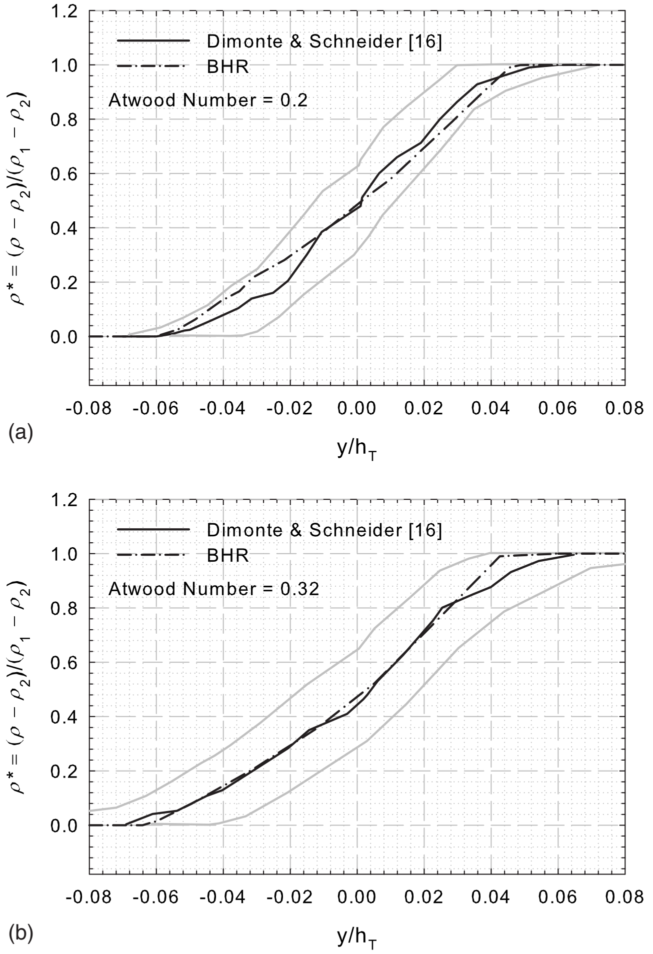

FIG. 8. Comparison of the BHR volume fraction profiles with the LEM experimental data of Dimonte and Schneider [16] at $A_t = 0.2$ (a) and $A_t = 0.32$ (b). The gray lines indicate the uncertainty bands from Dimonte and Schneider [16].

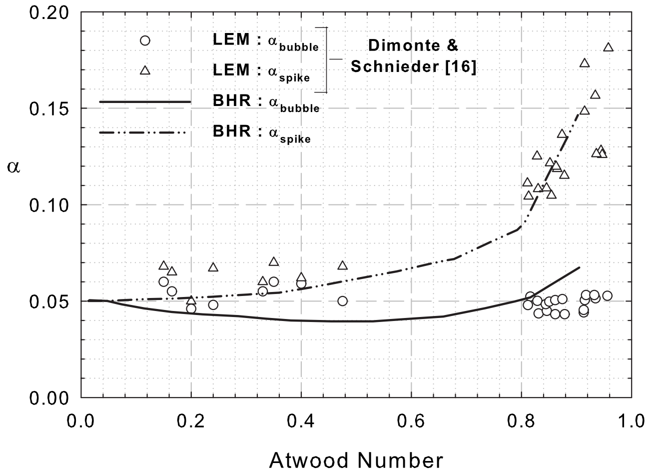

FIG. 9. Comparison of the growth constants (α_b & α_s) obtained from BHR model with the LEM experimental data of Dimonte and Schneider [16].

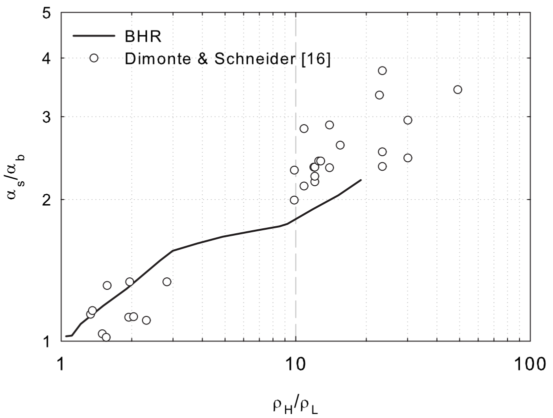

FIG. 10. Comparison of the ratio of growth constants (α_s/α_b) obtained from BHR model with the LEM experimental data of Dimonte and Schneider [16].

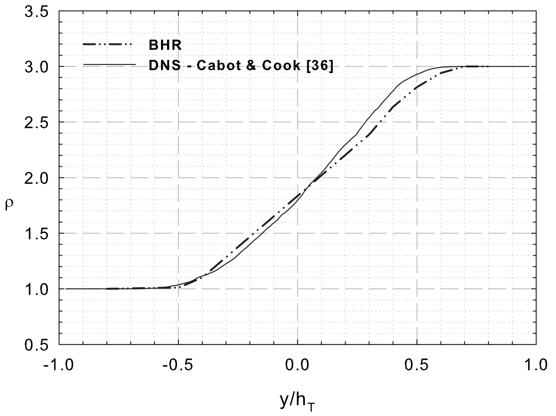

FIG. 11. Comparison of the density profiles obtained from BHR model with the DNS data of Cabot and Cook [36].

3. Comparison with RT direct numerical simulation (DNS)

The BHR *k-S-a* model was also compared with the large DNS (3072^3) data sets of Cabot and Cook [36] at $A_t = 0.5$, at three different times during the RT mix development. Figure 11 compares the density profiles across the mix obtained from the DNS with the BHR *k-S-a* data. As in earlier cases of comparison with experiments (Gas Channel and LEM), both sets of data show a linear variation for the mixture fraction was measured across the RT mixing layer, with slight rounding at the edges attributed to the shape of the plumes at the RT mix edge. The growth constant α was about 0.04 and was matched using a value of $C_4 = 0.8$ (see Table I). The turbulence kinetic energy profiles across the mix for both BHR *k-S-a* and DNS are compared in Fig. 12. It is seen that scaled profiles of k in DNS are approximately parabolic with a peak centered at the geometric centerline of the RT mixing layer. However, the k profiles obtained using BHR *k-S-a* model is slightly skewed with the peak occurring toward the spike side in agreement with the results of the 2-fluid model [23]. Similar asymmetries are observed for the plots of mass flux velocity, a, as seen in Fig. 13. The density self-correlation, b, across the mix is plotted in Fig. 14, and again the profile of b obtained from DNS is not symmetric with the peak skewed toward the spike side. Next we compare the length scale, S, profiles. We use the low Atwood number (∼0.01) DNS of Ristorcelli and Clark (2004) to fix a value σ_ε that would give good agreement between the DNS and the model simulations. Large changes in the value of σ_ε from 1.3 to a value of 0.1 were required to match the DNS length-scale distribution. Figure 15 plots the BHR *k-S-a* model runs with σ_ε set as 1.3 and 0.1, the low value of σ_ε ensured a top hat profile.We get good agreement with DNS for the smaller value of $\sigma_\varepsilon = 0.1$. This value of σ_ε was used throughout this work (see Table I). Figure 16 compares the BHR *k-S-a* length-scale profile (normalized by the total mix width) with the profile of S/W from the Cabot and Cook large Atwood DNS.

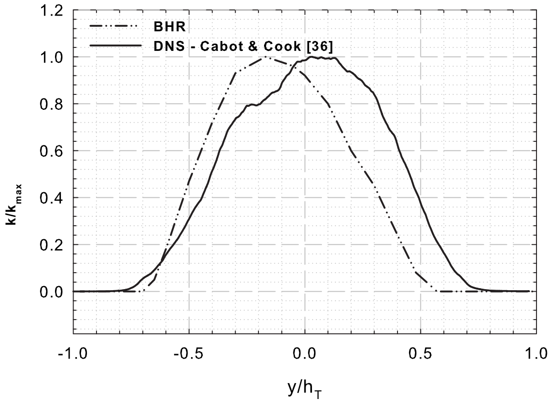

FIG. 12. Comparison of the normalized turbulent kinetic energy profiles obtained from BHR model with the DNS data of Cabot and Cook [36].

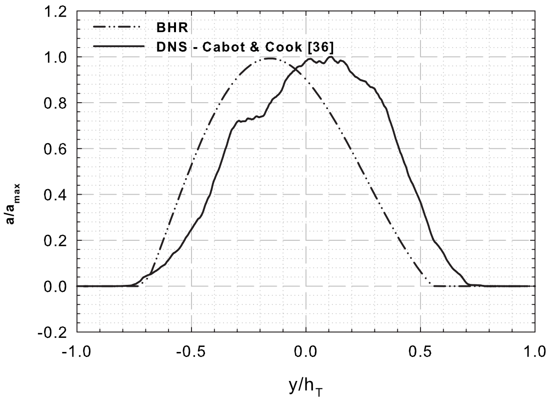

FIG. 13. Comparison of the normalized mass flux velocity profiles obtained from BHR model with the DNS data of Cabot and Cook [36].

C. RM instability (shock driven flow)

The BHR *k-S-a* model has also been applied to RM experiments in shock tubes using the standard values of coefficients listed in Table I. The RM experiments of Vetter and Sturtevant [38] used a shock tube which was 0.61 m long with a 0.267 m square test section. Shock Mach numbers (M_s) of 1.18 to 1.98 were generated in air that propagated toward a membrane (and mesh) at the interface of sodium

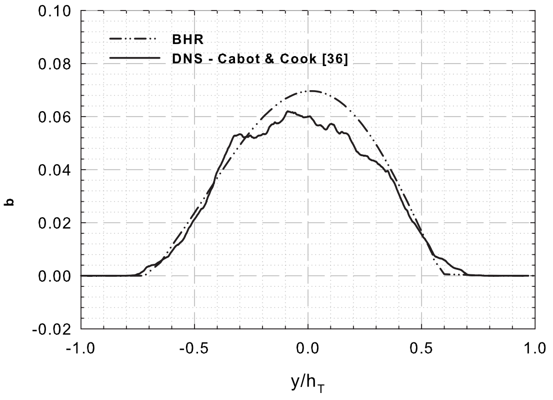

FIG. 14. Comparison of the density self-correlation profiles obtained from BHR model with the DNS data of Cabot and Cook [36].

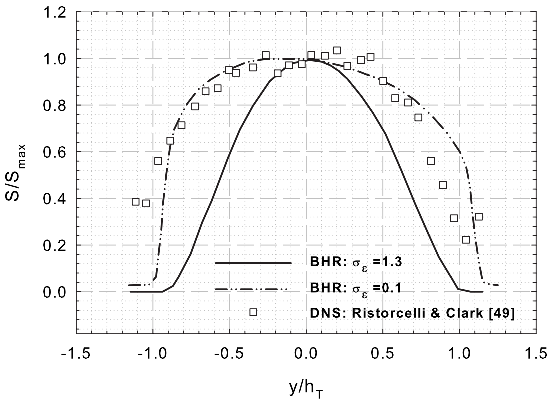

FIG. 15. Comparison of the length-scale profiles obtained from BHR model with the DNS data of Ristorcelli and Clark [49]. Large changes in original σ_ε were needed to match DNS data.

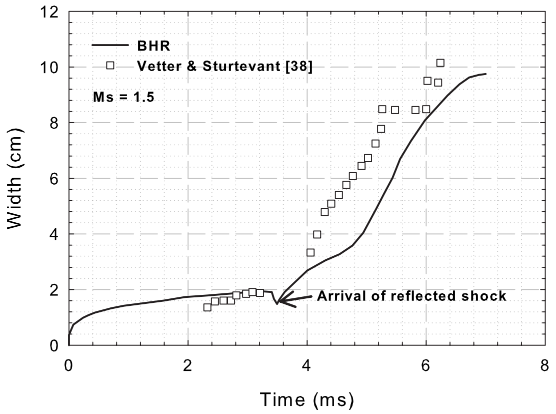

FIG. 17. Comparison of mix-widths at Ms=1.5 for the Vetter and Sturtevant [38] RM experiment.

hexafluoride (SF_6). Flow visualization was done using high-resolution Schlieren imaging where the light source was a single spark source that generated a flash of light in the visible spectrum for ~0.5 μs. The optical windows for the Schlieren visualization system were centered 0.42 m downstream of the membrane and were 0.15 m in diameter. We compared BHR simulations with experimental data at M_s =1.24 (run no. 88), 1.5 (run no. 85) and 1.98 (run no. 87), as they have the most data points and images. Figure 17 plots the growth of the interfacial perturbations measured from Schlieren imaging for a Mach 1.5 shock. The mixing zone grows to ~2 cm before the transmitted shock gets reflected from the end wall and reshocks it ~3.4 ms. The growth rate from the re-shock exceeds that from the initial shock as the perturbations (initial amplitudes) are larger. The BHR model calculations, denoted by solid lines, exhibit an identical behavior with similar growth rates as that of the experiment. Figure 18 plots the mix width from the Mach 1.24 shock experiment. Little growth (<2 cm) is observed before the shock interacts with the interface (~9.5 ms). The growth of interface between the reflected shock and the arrival of the reflected expansion wave appears to be linear for both the experiment (dots) and the BHR simulations (solid line). For the Mach 1.98 shock experiment, the BHR simulations deviate from the experimental results, as seen in Fig. 19, especially for the data points following reshock. This mismatch in data can be attributed to experimental uncertainty of the mixing width measurements and the ability to characterize exact initial conditions in the BHR *k*-*S*-*a* simulations over the range of shock Mach numbers of the experiments.

It is evident from above that initial conditions play a significant role in the RM experiments. So, the effect of initial conditions on the BHR *k*-*S*-*a* simulations of RM was studied by varying the initial length scale (S_0) in the model. This mimics experimental differences due to different meshes and membrane-mesh ordering. Vetter and Sturtevant [38] studied the influence of membrane placement relative to the mesh on the mixing for Mach 1.5 shock experiments. In the first configuration, the membrane was placed on the downstream side of the mesh, and in the second configuration the order of the mesh and membrane was reversed. Reversing the order of the mesh and the membrane, with the membrane being on the upstream side, introduced a perturbation to the interface. This resulted in a dramatic increase in growth rates between the two cases. The BHR *k*-*S*-*a* model captured this variation in the initial perturbations by varying the initial length scale (S_0) by a factor of 10 from a value of 0.1 to 1.0, as the results in Fig. 20 shows, BHR *k*-*S*-*a* gives reasonably good agreement between experimental (dots and squares) data and the model simulation (solid line).

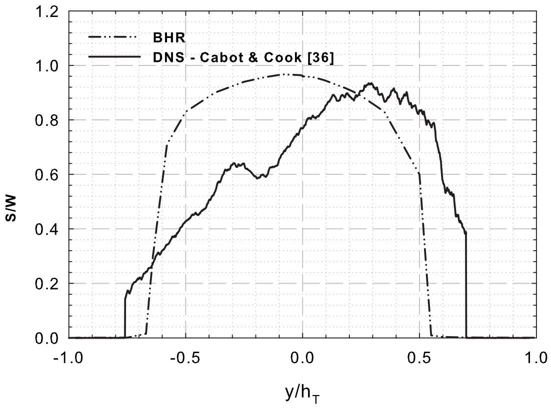

FIG. 16. Comparison of the length-scale profiles obtained from BHR model with the DNS data of Cabot and Cook [36].

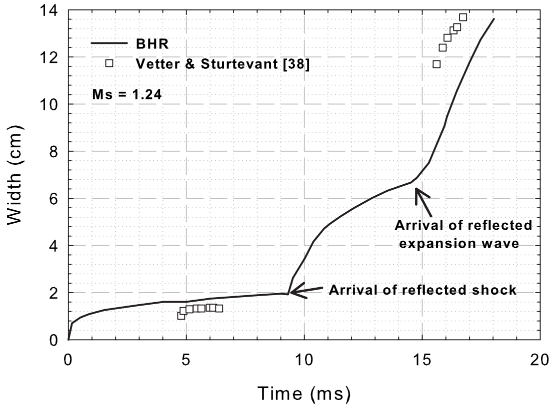

FIG. 18. Comparison of mix-widths at Ms=1.24 for the Vetter and Sturtevant [38] RM experiment.

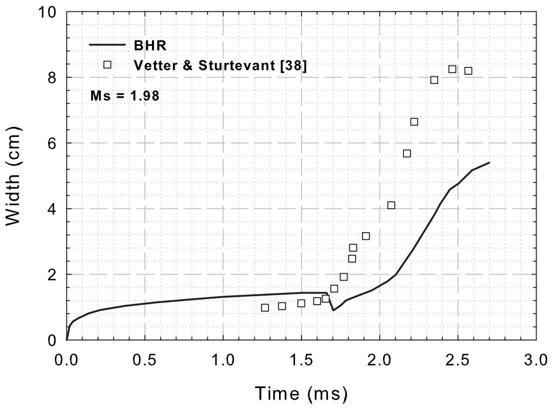

FIG. 19. Comparison of mix-widths at Ms=1.98 for the Vetter and Sturtevant [38] RM experiment.

The BHR *k*-*S*-*a* model was also applied to the shock tube experiments of Poggi *et al.* [37] that were conducted in a test section 0.3 m long, with a 8 cm square cross section. A Mach 1.45 shock was incident in SF_6, and the downstream fluid (air) was separated by a thin membrane supported by a mesh. The location of the origin was the initial position of the interface, and the time origin corresponded to the incident shock wave crossing this location. The time evolution of the locations is plotted in Fig. 21(a), with dots denoting the mixing zone edges from the experiment (based on a 5–95 % definition). We find good agreement between the BHR *k*-*S*-*a* simulation and the experimental results. The width of the BHR *k*-*S*-*a* computed turbulent mixing zone is compared with experimental measurement in Fig. 21(b) revealing good agreement between the two results. Laser doppler anemometry (LDA) probes were located at various downstream locations [denoted by squares in Fig. 21(a) and 21(b)] giving measurements of turbulence intensities in the mixing zone before and after shock crossing, and also quantified the turbulence decrease between two interactions of the shock waves. Next, in Figs. 22(a)–22(d), the BHR *k*-*S*-*a* simulation is compared with the experimental results obtained at four downstream locations of 51, 161, 169, and 178.5 mm (as they have most data points). The axial variance $\overline{u'^2}$ as a function is compared at these four locations along the RM mixing zone. At 51 mm, Poggi *et al.* [37] divided the period (~51 μs) into three samples to obtain a profile of $\overline{u'^2}$ with a statistical error of ±23%. On comparison of BHR *k*-*S*-*a* simulations with the experimental results [see Figs. 22(a)–22(d)], we see that the variance $\overline{u'^2}$ is of the same order of magnitude for all the cases. The mixing zone at this location has been generated by RMI as the incident shock wave goes through the interface. At further downstream locations, i.e., 161, 169, and 178.5 mm, both the experiment and BHR *k*-*S*-*a* simulation predict a strong increase in the axial velocity variance $\overline{u'^2}$, with the velocity variance reaching a peak value at 161 mm followed by a global decrease of $\overline{u'^2}$. However, the axial velocity variance predicted by the BHR *k*-*S*-*a* simulation is about a factor of 2 higher than the experimental data at these three downstream locations. Indeed, between the locations of 161 and 178.5 mm, there is no significant turbulence production and diffusion, and dissipation is the dominant mechanism in the flow. Figure 23 plots the modeled production and dissipation terms at t=0.3 μs, 0.1 ms, and 3.0 ms after the first shock passes through the interface. At early times, i.e., t=0.3 μs, the buoyancy production term dominates. However at late times (t=1.0 and 3.0 ms), dissipation is the dominating mechanism.

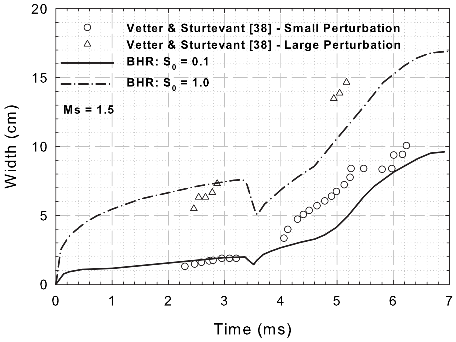

FIG. 20. Effect of initial conditions for the BHR RM simulations. Comparison of mix-widths at Ms=1.5 for the Vetter and Sturtevant [38] RM experiment.

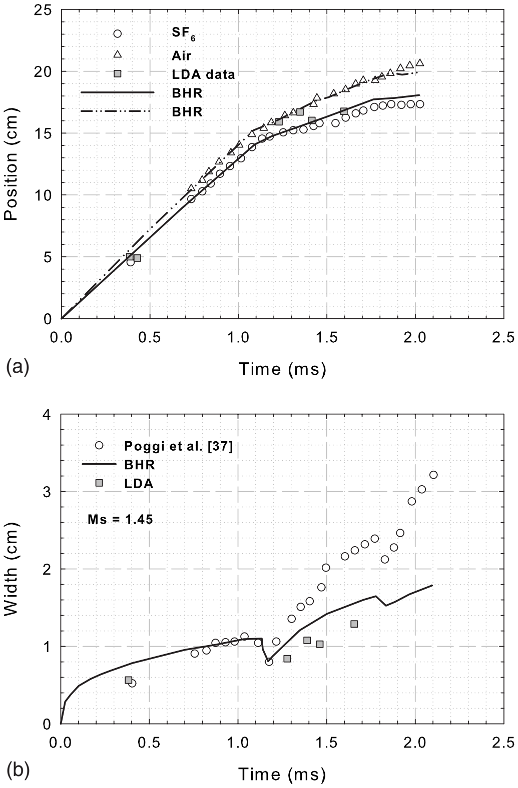

FIG. 21. Comparison of the interface positions (a) and mix-widths (b) at Ms=1.45 for the Poggi *et al.* [37] RM experiment.

V. CONCLUDING REMARKS

The BHR *k*-*S*-*a* model implemented in the RAGE hydrocode has been used to describe the self-similar growth of KH, RT and RM instabilities. The mean hydrodynamics equations for a single phase fluid have been supplemented by

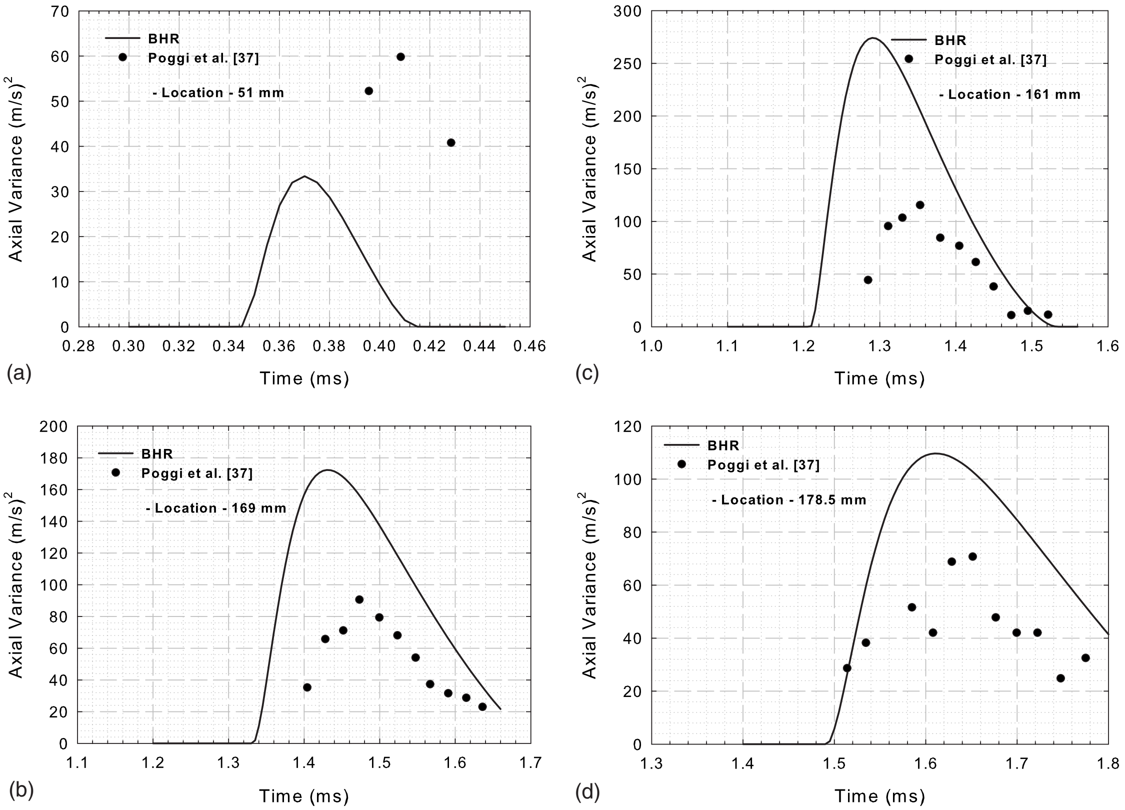

FIG. 22. Comparison of turbulent intensities at various downstream locations (a) 51 mm, (b) 161 mm, (c) 169 mm and (d) 178.5 mm for the Poggi *et al.* [37] RM experiment with BHR simulation at Ms=1.45.

evolution equations for turbulent kinetic energy (k), length scale of the dominant eddies (S), and a mass-flux velocity (a), and an algebraic closure for density self-correlation (b). Unknown model constants were determined from experimental data by analytical self-similar solutions (for the RT case), and by iterative matching to simulate experimental results (for the KH and RM case). The BHR k-S-a model was used to quantitatively describe a variety of turbulence experiments and numerical simulations of turbulent flows, that includes low speed shear layer flow, RT flows over a wide range of Atwood numbers, and a moderate Atwood number DNS of RT flows. Accurate prediction of these flows is important because they occur in ICF implosions, supernova explosions, buoyant jets, and combustion applications. The aim of the model was to generate results that provide the overall trends for many different classes of flows. The BHR k-S-a model has been shown to do well when predicting free and compressible shear flow experiments, RT growth rates over a wide range of Atwood numbers, as well as predicting RM growth rates prior to reshock. However, it does a reasonable job in RM flow post reshock, and does not allow demixing on reversal of a driving force (gravity). Future model improvements may be considered that would involve a nongradient diffusion based multispecies concentration equation that would allow demixing. Also, improved forms of Boussinesq approximation may be used for improvement in early time and reshock environments. Future work might also pursue additional experiments and DNS to test the model under a wider variety of test cases (demix, variable acceleration, impulsive acceleration, multilayer problems, etc.) and thus understand the effects of initial conditions, convergent geometries as well as more complex flows.

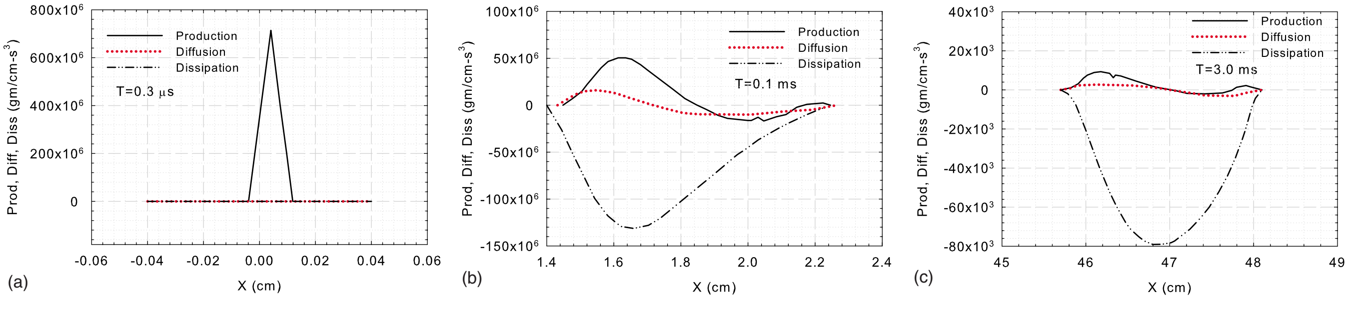

FIG. 23. (Color online) Comparison of the production (red), diffusion (black) and dissipation (blue) terms at three different times after the first shock (prior to re-shock).

[1] H. L. F. v. Helmholtz, *Über discontinuierliche Flüssigkeits-Bewegungen [On the discontinuous movements of fluids].* Monatsberichte der Königlichen Preussiche Akademie der Wissenschaften zu Berlin [Monthly Reports of the Royal Prussian Academy of Philosophy in Berlin], 1868. Vol. 23, p. 215.

[2] L. Kelvin, Philos. Mag. **42**, 362 (1871).

[3] L. Rayleigh, Proc. R. Soc. London **14**, 170 (1884).

[4] G. I. Taylor, Proc. R. Soc. London, Ser. A **201**, 192 (1950).

[5] E. E. Meshkov, Soviet Fluid Dynamics **4**, 101 (1969).

[6] R. D. Richtmyer, Commun. Pure Appl. Math. **13**, 297 (1960).

[7] J. D. Lindl, Phys. Plasmas **2**, 3933 (1995).

[8] J. D. Lindl, *Inertial Confinement Fusion: The Quest for Ignition and Energy Gain using Indirect Drive* (Springer, Berlin, 1998).

[9] S. F. Gull, Mon. Not. R. Astron. Soc. **171**, 263 (1975).

[10] P. Marmottant and E. Villermaux, J. Fluid Mech. **498**, 73 (2004).

[11] O. A. Molchanov, Phys. Chem. Earth **29**, 559 (2003).

[12] A. M. Khokhlov, E. S. Oran, and G. O. Thomas, Combust. Flame **117**, 323 (1999).

[13] D. C. Besnard *et al.*, Los Alamos National Laboratory Report No. LAUR-12303, 1992 (unpublished).

[14] U. Alon *et al.*, Phys. Rev. Lett. **74**, 534 (1995).

[15] B. Cheng, J. Glimm, and D. H. Sharp, Chaos **12**, 267 (2002).

[16] G. Dimonte and M. Schneider, Phys. Fluids **12**, 304 (2000).

[17] Y. Zhou, G. B. Zimmerman, and E. W. Burke, Phys. Rev. E **65**, 056303 (2002).

[18] V.S. Smeeton, and D. L. Youngs, *Experimental Investigation of Turbulent Mixing by Rayleigh-Taylor Instability*. 1987, AWRE Report.

[19] L.G. Stafford, *An experimental investigation of turbulent mixing due to buoyancy forces in unstably stratified media*. 1982, CFDU report.

[20] Y. A. Kucherenko, V. E. Neuvazhaev, and A. P. Pylaev, Phys. Dokl. **39**, 114 (1994) Official English Translation of Doklady Akademii Nauk.

[21] N. Freed *et al.*, Phys. Fluids A **3**, 912 (1991).

[22] A. J. Scannapieco and B. L. Cheng, Phys. Lett. A **299**, 49 (2002).

[23] D. L. Youngs, Physica D **37**, 270 (1989).

[24] D. L. Youngs, Physica D **12**, 32 (1984).

[25] D. L. Youngs, *Experimental Investigation of Turbulent Mixing by Rayleigh-Taylor Instability*, Advances in Compressible Turbulent Mixing, edited by W. P. Dannevik, A. C. Buckingham, and C. E. Leith (National Technical Information Service, US Department of Commerce, Princeton, New Jersey, 1992), pp. 607–626.

[26] K. I. Read, Physica D **12**, 45 (1984).

[27] M. J. Andrews, *The k-ε* model applied to the development of Rayleigh-Taylor instability, in *Phoenics Demonstration Report*. 1984.

[28] M. J. Andrews, *Mechanical Engineering* (Imperial College, London, 1986).

[29] Y. Zhou *et al.*, Astron. Astrophys. **405**, 379 (2003).

[30] G. Dimonte and R. Tipton, Phys. Fluids **18**, 085101 (2006).

[31] S. Gauthier and M. Bonnet, Phys. Fluids A **2**, 1685 (1990).

[32] D. M. Snider and M. J. Andrews, ASME J. Fluids Eng. **118**, 370 (1996).

[33] D. C. Besnard, F. H. Harlow, and R. M. Rauenzahn, Los Alamos National Laboratory Report No. LA-10911-MS, 1987.

[34] O. Grégoire, D. Souffland, and S. Gauthier, J. Turbul. **6**, N29 (2005).

[35] A. Banerjee, W. N. Kraft, and M. J. Andrews, J. Fluid Mech. **659**, 127 (2010).

[36] W. H. Cabot and A. W. Cook, Nat. Phys. **2**, 562 (2006).

[37] F. Poggi, M.-H. Thorembey, and G. Rodriguez, Phys. Fluids **10**, 2698 (1998).

[38] M. Vetter and B. Sturtevant, Shock Waves **4**, 247 (1995).

[39] J. H. Bell and R. D. Mehta, AIAA J. **28**, 2034 (1990).

[40] G. S. Elliott and M. Samimy, Phys. Fluids A **2**, 1231 (1990).

[41] P. Chassaing, Flow, Turbul. Combust. **66**, 293 (2001).

[42] P. Chassaing, *Variable Density Fluid Turbulence: Fluid Mechanics and Its Applications* (Kluwer Academic Publishers, Dordrecht, Boston, 2002), Vol. 69.

[43] K. Hanjalić, Annu. Rev. Fluid Mech. **34**, 321 (2002).

[44] M. J. Steinkamp, *Spectral Analysis of the Turbulent Mixing of Two Fluids*, Nuclear Engineering (University of Illinois at Urbana-Champaign, Urbana, IL, 1995).

[45] R. M. Baltrusaitis *et al.*, Phys. Fluids **8**, 2471 (1996).

[46] P. B. Spitz and J. F. Haas, *Proceedings of 3rd International Workshop on the Physics of Compressible Turbulent Mixing* (CEA DAM, Villeneuve St.-George, France, 1991).

[47] A. Banerjee and M. J. Andrews, Phys. Fluids **18**, 035107 (2006).

[48] A. Banerjee, *Mechanical Engineering* (Texas A&M University, College Station, TX, 2006).

[49] J. R. Ristorcelli and T. T. Clark, J. Fluid Mech. **507**, 213 (2004).

[50] Y. Zhou, Phys. Plasmas **14**, 082701 (2007).

[51] Y. Zhou *et al.*, Phys. Plasmas **10**, 1883 (2003).

[52] Y. Zhou, H. F. Robey, and A. C. Buckingham, Phys. Rev. E **67**, 056305 (2003).

[53] A. Banerjee and M. J. Andrews, Int. J. Heat Mass Transfer **52**, 3906 (2009).